

Article

# Electromagnetic–Mechanical Coupling Optimization of an IPM Synchronous Machine with Multi Flux Barriers

Wenye Wu <sup>1,\*</sup> , Qingzhang Chen <sup>1,\*</sup>, Xiaoyong Zhu <sup>2</sup>, Fuzhou Zhao <sup>1</sup> and Zixuan Xiang <sup>2</sup>

<sup>1</sup> School of Automotive Engineering, Changshu Institute of Technology, Suzhou 215500, China; xjz2020@163.com

<sup>2</sup> School of Electrical and Information Engineering, Jiangsu University, Zhenjiang 212013, China; zxyff@ujs.edu.cn (X.Z.); zxxiang@ujs.edu.cn (Z.X.)

\* Correspondence: wwyzhshsh0308@163.com (W.W.); cqz@cslg.edu.cn (Q.C.)

Received: 21 February 2020; Accepted: 6 April 2020; Published: 9 April 2020



**Abstract:** In this paper, an interior permanent magnet (IPM) synchronous machine with multiflux barriers is proposed to meet the wide speed regulation application requirements of electric vehicles. Based on the flux barrier characteristic, an electromagnetic–mechanical coupling optimization strategy is employed for the machine design. In order to facilitate the optimization design, the rotor barriers are divided into two optimization zones, the maximum stress zone and the maximum deformation zone. The electromagnetic–mechanical coupling optimization strategy is divided into two stages accordingly. In the first stage, the machine is regarded as a synchronous reluctance machine by ignoring permanent magnets, where the dimensions of the arc-shaped barriers are optimized to achieve a large reluctance torque and small stress. In the second stage, the dimensions of the arc-shaped PMs and the elliptical barrier are optimized with three objectives of minimum torque ripple, minimum flux linkage, and minimum deformation. After machine optimization, the comparison investigations are carried out on the basis of finite-element analysis by considering both the electromagnetic performances and mechanical performances.

**Keywords:** IPM machine; mechanical characteristics; multi flux barriers; coupling optimization method

## 1. Introduction

In recent years, with the rise of electric vehicles, considerable attention has been focused on interior permanent magnet (IPM) synchronous machines' design and optimization [1,2]. Theoretically, an IPM synchronous machine can be operated with wide or even infinite speed ranges for constant power operation using the flux weakening control method [3]. However, due to the increase of centrifugal force in rotor bridges, the problem of insufficient mechanical strength often becomes particularly acute when the machines operate at high speed. It is worth noting that the situation may become more severe when it comes to a machine with multiflux barriers in its rotor. Research has implied that the layout of flux bridges and flux barriers in IPM synchronous machines not only affects the electromagnetic characteristics but also determines the mechanical reliability of machines at high speeds [4,5]. Therefore, the correct method of designing a suitable IPM machine to meet the high-speed operation of electric vehicles is still a great challenge.

Electric vehicles often need to operate in different driving conditions, such as low-speed driving conditions in cities and medium-to-high speed driving conditions in the suburbs; thus, a wide range of speed regulation is generally required for their driving machine [6,7]. Whereas with regard to IPM synchronous machines, there are natural permanent magnets in their rotors, the constant PM potential often makes it difficult to adjust the air-gap magnetic field. This results in certain defects in

the speed regulation for IPM synchronous machines [8,9]. To remedy this situation, by expanding the  $d$ - $q$  inductance difference, designing the air flux barriers in PM machine rotor has been proven to be a viable method. Some researchers have involved the exploration of rotor flux barrier design. In [10–12], a type of PM-assisted synchronous REL machine is proposed for variable speed applications. The main characteristic of this type of machine is that several flux barriers per pole are adopted in rotor configuration. A higher saliency ratio caused by the several flux barriers allows a lower level of PM flux linkage. As a result, it is easier for this type of machine to offset the magnetic forces of the  $d$ -axis. Another advantage of the rotor flux barriers is the great contribution of reluctance torque to total output torque. In addition, another kind of multflux-barrier machine with the characteristic of a flux-intensifying effect is also proposed and has attracted much attention [13–15]. Different from those in PM-assisted machines, the multflux barriers in flux-intensifying PM machines are set in a rotor  $q$ -axis rather than  $d$ -axis, which results in the unique characteristic of  $d$ -axis inductance  $L_d$  which is greater than the  $q$ -axis inductance  $L_q$ . Initial research has shown that the flux-intensifying effect can contribute to realizing the high-speed cruise with a reduced flux-weakening current, which can reduce the risk of irreversible demagnetization and widen the speed range as well. Although there have been a lot of reports on the design of rotor flux barriers, these studies are mainly focused on the proposal of new machines, seldom involving the flux barrier design methods. Therefore, research on the design methods of the IPM machine with multirotor flux barriers becomes extremely important.

Currently, the machine design and optimization are often estimated individually using the electromagnetic field analysis method and stress analysis method, respectively. Few studies have dealt with the design of high-speed machines by considering the combination of electromagnetic and mechanical characteristics [16]. In this paper, to meet the requirements of electric vehicle (EV) applications, a new IPM synchronous machine with multflux barriers is proposed and optimized. In the optimization process, the barrier partition strategy is applied to improve optimization efficiency. Both electromagnetic performances and mechanical performances are considered as optimization objectives in the partition optimization. Additionally, the performances of the machine before and after optimization are also discussed at the last part of the paper.

## 2. Machine Structure and Stress Analysis

As illustrated in Figure 1, the proposed machine rotor is characterized by two layers of arc-shaped barriers and one ellipse-shaped barrier in each pole, and hence, a relatively large reluctance torque can be generated in this machine. Further, in order to improve the power factor and torque output capacity of the machine, arc-shaped PMs are inserted into the two layers of arc-shaped barriers. As it is a machine for EVs, wide speed range and high-speed capability are generally required. Therefore, both the central rib and end rib are set to guarantee the rotor integrity and improve rotor strength at high-speed operation, since a large centrifugal force will cause great damage to the weak areas of the rotor in this state. The specific machine parameters and material properties are shown in Tables 1 and 2.

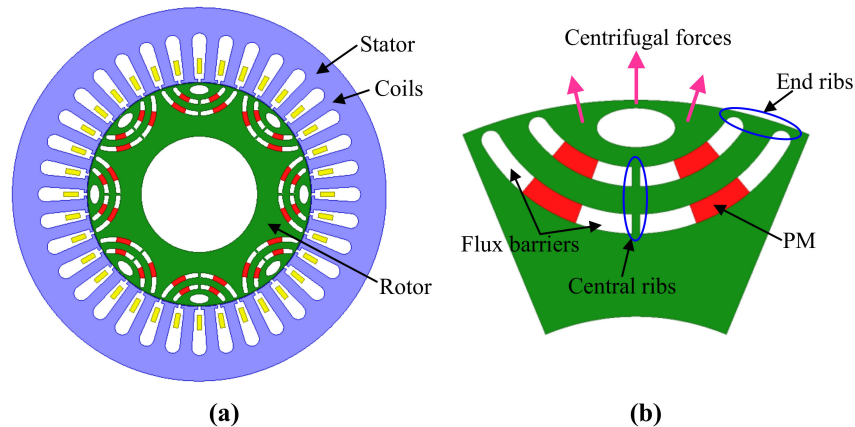
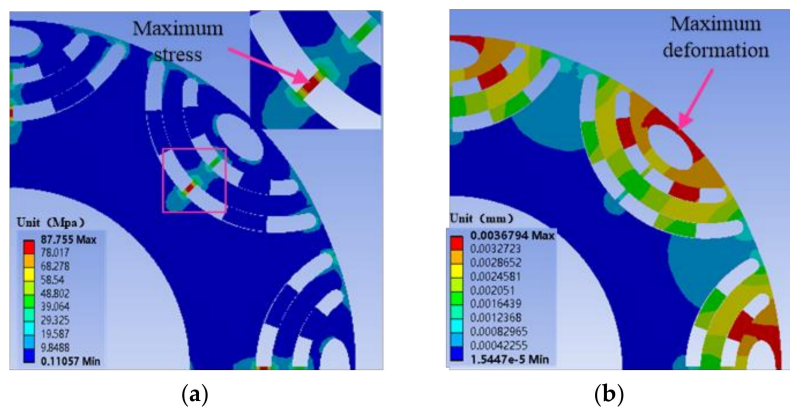
In this section, in order to explore the influence of the centrifugal force on the structure strength of machine, static structural analysis of the machine rotor is carried out by the Workbench 16.1 under the condition that the maximum machine speed is 10000 rpm, and the corresponding simulation results are shown in Figure 2.

**Table 1.** Main design specifications of the machine.

Parameters	Values	Parameters	Values
Rated power	5.5 kW	Inner diameter	116 mm
Rated speed	1200 rpm	Stack length	65 mm
Maximum speed	10,000 rpm	Air gap	0.5 mm
Rated torque	40 Nm	Number of turns	16
Outside diameter	195 mm	PM property	NdFeB (1.2T)

**Table 2.** Material properties of the permanent magnet (PM) and rotor core.

Materials	Density	Young's Modulus	Poisson's Ratio
	kg/m <sup>3</sup>	GPa	/
PM	7400	150	0.23
Rotor core	7650	200	0.3

**Figure 1.** Machine and its rotor details: (a) the whole machine structure; (b) machine local structure and force characteristics.**Figure 2.** Rotor mechanical properties at the rotor speed of 10000 rpm: (a) stress analysis; (b) deformation analysis.

From Figure 2a,b, it can be found that the maximum stress point and the maximum deformation point do not occur in the same rotor zone. The maximum stress point of the rotor is located in the center ribs of the lower arc-shaped barrier, while the maximum deformation of the rotor occurs on the ribs between the ellipse-shaped barrier and the air gap. Therefore, it is very necessary to consider the maximum stress zone and the maximum deformation zone separately in the optimization design process.

### 3. Electromagnetic–Mechanical Coupling Optimization

#### 3.1. Optimization Strategy

According to the mechanical analysis in the previous section, it is known that the maximum stress zone does not coincide with the maximum deformation zone. Therefore, to improve the efficiency of optimization, it is very necessary to divide the rotor barriers into subzones and optimize it step by step. Based on this, the rotor barriers are divided into two subzones, maximum stress zone and maximum deformation zone. The specific zone division and the related parameters are illustrated in Figure 3.

In particular, the maximum stress zone is mainly determined by the dimensions of the two layers of arc-shaped barriers, and the maximum deformation zone is mainly determined by the dimensions of the ellipse-shaped barrier and PM pieces. Hence, the process of optimization design is divided into two steps accordingly. In the first step, the machine is regarded as a synchronous reluctance machine by ignoring permanent magnets, where the dimension parameters of arc barriers, such as end rib  $Rib_1$ , upper barrier thickness  $h_2$ , lower barrier thickness  $h_1$ , and center rib  $Rib_2$  are selected as design variables. In the second step, arc PM pieces are inserted into rotor flux barriers to produce a PM-assisted synchronous machine. In this step, the starting angle of arc PM in barrier  $\beta_{po}$ , the radian of the PM in barrier  $\beta_{pm}$ , the length of the major axis of the elliptical barrier of  $a$ , and the proportion coefficient of minor axis and major axis of  $R$  are selected as design variables. The specific optimization steps and variable variation ranges are listed in Table 3.

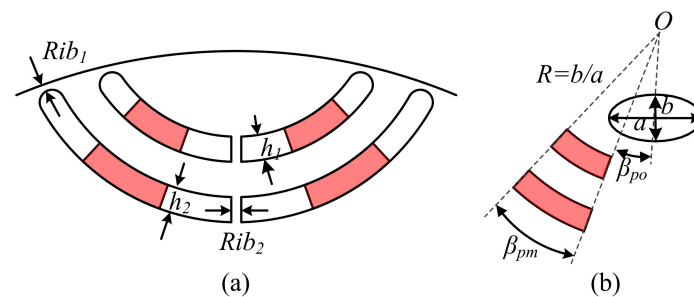


**Figure 3.** Geometric parameters: (a) The parameters related to the maximum stress zone. (b) The parameters related to the maximum deformation zone.

**Table 3.** Optimization process.

Steps	Objectives	Variables and Variation Ranges
1	Reluctance torque ( $T_{rel}$ ) Saliency ratio ( $\xi$ ) Maximum stress ( $\tau$ )	$Rib_1$ : 0.5–2.0 mm $Rib_2$ : 0.5–2.0 mm $h_1$ : 1.5–3.5 mm $h_2$ : 1.5–3.5 mm
2	Flux linkage ( $\psi$ ) Torque ripple ( $T_{ripple}$ ) Maximum deformation ( $\gamma$ )	$\beta_{pm}$ : 14–28° $\beta_{po}$ : 5–30° $R$ : 0.2–0.5 $a$ : 2.0–6.0 mm

### 3.2. Objectives, Objective Functions, and Constraints

Considering the potential applications in electric vehicles, high-output torque is generally required to realize the frequent acceleration, deceleration, and overloaded climbing. In addition, to improve system stability and comfort, the performance of low torque ripple is also required. It is worth mentioning that the mechanical strength of machine rotor also needs to emphatically consider when EVs are operating at high speed.

#### 3.2.1. Maximum Stress Coupling Optimization Zone

In this zone, the structure of the two layers of arc-shaped barriers does not only affect the maximum stress in the center ribs but also has an important influence on the reluctance torque, because the variations of barrier shape will determine the variations of the inductance in the  $d$ -axis and  $q$ -axis, that is, the rotor saliency ratio. Thus, the maximum stress, saliency ratio, and reluctance torque are set as objectives in this step. The corresponding objective function and its constraints are given as follows:

$$\begin{cases} \text{Function : } [Max f(T_{rel}), Max f(\xi), Min f(\tau)] \\ \text{Constraints : } T_{rel} \geq 0.6T_{out}, \tau \leq 80Mpa \end{cases} \quad (1)$$

where  $\text{Max } f(T_{rel})$ ,  $\text{Min } f(\xi)$ , and  $\text{Min } f(\tau)$  are the objective functions of reluctance torque, saliency ratio, and maximum stress.  $T_{out}$  is the output torque of the machine.

### 3.2.2. Maximum Deformation Coupling Optimization Zone

By inserting the PM pieces into flux barriers, a part of PM torque will be produced to increase the output torque. Meanwhile, due to the attraction of PM and magnetic steel of the rotor, the addition of PM pieces will partially change the deformation around the elliptical barrier. Thus, the PM flux linkage and maximum deformation are selected as objectives. In addition, to ensure the stability of machine torque output, the torque ripple is also identified as an optimization objective. The corresponding objective function in this step and its constraints are given as follows:

$$\begin{cases} \text{Function : } [\text{Min } f(\psi), \text{Min } f(T_{ripple}), \text{Min } f(\gamma)] \\ \text{Constraints : } T_{ripple} \leq 0.08, \gamma \leq 0.3\mu\text{m} \end{cases} \quad (2)$$

where the  $\text{Max } f(\psi)$ ,  $\text{Min } f(T_{ripple})$ , and  $\text{Min } f(\gamma)$  are the objective functions of flux linkage, torque ripple, and maximum deformation.

### 3.3. Boundary Conditions, Loads, and Solution

Since this research deals with the optimization of mechanical and electromagnetic coupling problems, the boundary condition setting, loading, and meshing are also divided into the electromagnetic part and mechanical part. In electromagnetic simulation, an air region is created to wrap the entire machine, and then the outer boundary of the air region is set as vector potential. The machine is loaded in the form of current excitation, in which the excitation current amplitude is 40 A. In addition, since adaptive mesh generation usually results in long computation time, the rotor near the air gap is divided into multiple layers, where it is segmented by surface approximation. In electromagnetic simulation, in order to obtain the stress and strain of rotor more accurately, the connections between the rotor and magnets are set as bonded connections as relative sliding is not expected. Figure 4 gives the grid subdivision and loading method in mechanical structure simulation. It can be seen that the rotor part and the magnet parts adopt different size grid cells, and the load is inserted by giving a rotational velocity. Furthermore, for the rotor to rotate effectively, remote displacement support is applied to constrain the rotor part.

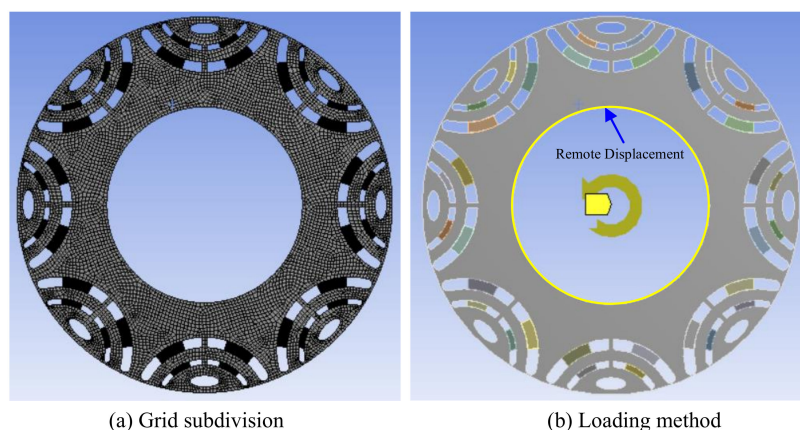


**Figure 4.** Settings in mechanical simulation: (a) grid subdivision; (b) loading method.

### 3.4. Optimization Step 1

Since each design variable may have different influences or sensitivities on the different design objectives during the process of machine design, the corresponding sensitivity index  $S(x_i)$  can be given by [17]

$$S(x_i) = \frac{V(E(y/x_i))}{V(y)} \quad (3)$$

where  $y$  is the optimization objective,  $E(y/x_i)$  is the average value of  $y$  when  $x_i$  is constant,  $V(E(y/x_i))$  is the variance of  $E(y/x_i)$ , and  $V(y)$  is the variance of  $y$ . Generally, a large value of  $S(x_i)$  implies a high effect on the optimization objective. The positive sensitivity index indicates that the optimization objective will increase with the growth of the design variable, while the negative one means a contrary variation [18]. Thus, the sensitivity of each design variable in step 1 on the optimization objectives can be calculated based on Equation (3) and illustrated in Figure 5.

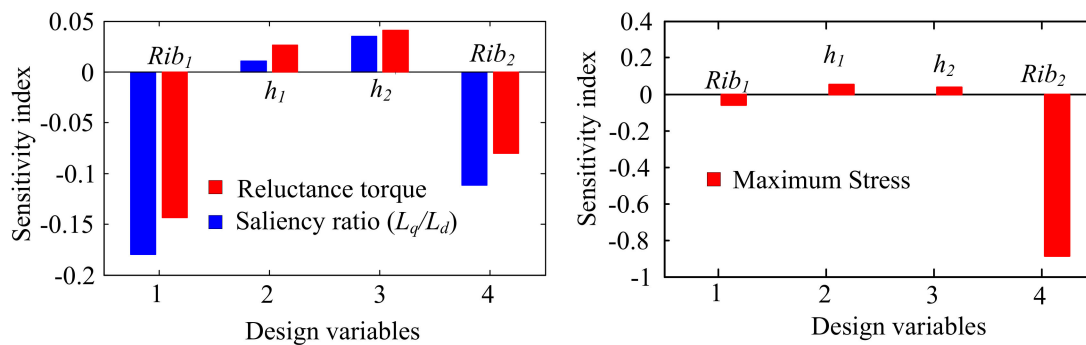


Figure 5. Sensitivity of the design variables on the optimization objectives.

It can be seen from the results of the sensitivity analysis that each variable presents different sensitivities to the optimization objectives. For electromagnetic performances, the effect of the end rib of  $Rib_1$  and center rib of  $Rib_2$  on the objectives of saliency ratio and reluctance torque is greater than the thickness of the barrier of  $h_1$  and  $h_2$ . For mechanical performances,  $Rib_2$  has the greatest effect on mechanical stress. More specifically, a smaller mechanical stress means a smaller machine saliency ratio, which is not conducive to the increase of machine reluctance torque. Therefore, a tradeoff between torque and mechanical properties is required.

Figure 6 shows the tradeoff between rotor saliency ratio and reluctance torque; it can be seen that there is a linear relation between saliency ratio and reluctance torque. That is, larger saliency represents higher reluctance torque. In order to make the reluctance torque reach 60% of the total torque, the feasible zone is preliminarily identified in the blue dots by the tradeoff of rotor saliency and reluctance. Due to the linear relationship between the saliency ratio and the reluctance torque, it is reasonable to determine the optimal design points through the tradeoff of saliency ratio and the mechanical stress. As illustrated in Figure 7, the optimal point is finally determined on the feasible design line, and the corresponding optimization variables of  $Rib_1$ ,  $Rib_2$ ,  $h_1$ , and  $h_2$  are 0.6, 1.5, 1.8, and 3.2 mm.

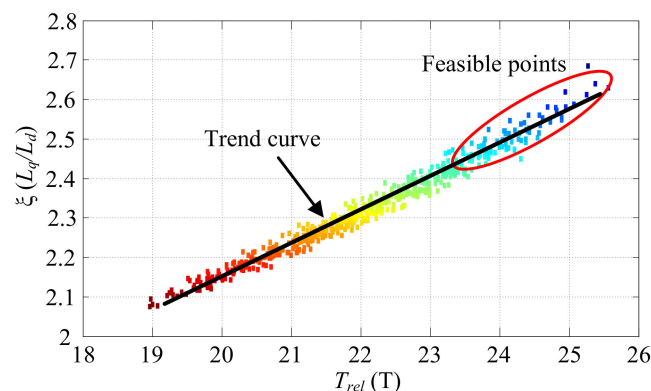
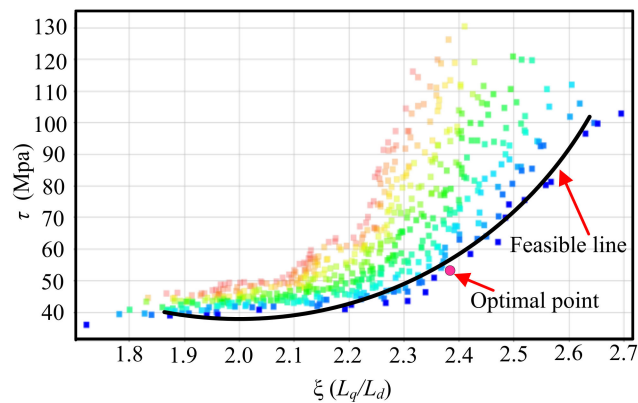


Figure 6. The tradeoff between rotor saliency ratio and reluctance torque.



**Figure 7.** The tradeoff between the maximum stress and the rotor saliency.

### 3.5. Optimization Step 2

Figure 8 shows the interacting influences of the three optimization objectives with the variations of the design variables. It can be observed that there are some conflicts among the three optimization objectives. In particular, for the parameters of  $a$  and  $R$  that specify the size of the elliptical barrier, which has an important relationship with the maximum deformation, whereas the effect of the two parameters on the flux linkage is very low. By contrast, the parameters of  $\beta_{po}$  and  $\beta_{pm}$  that specify the PM size have a great effect on flux linkage, but the effect on maximum deformation is relatively small. Additionally, with the exception of parameter of  $\beta_{pm}$ , all the other three parameters have a great influence on the torque ripple of the machine.

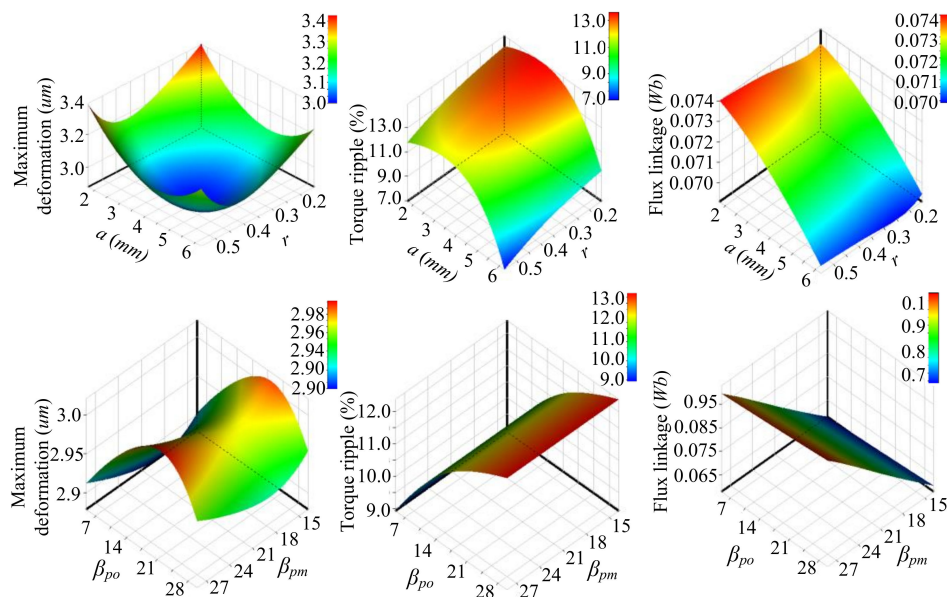


**Figure 8.** Response surface analysis of different optimization objectives versus design variables.

To overcome such contradictions, a trade-off design among the three optimization objectives is needed in step 2 design. Thus, a similar sequential nonlinear programming (SNP) algorithm method is adopted to this stage of optimization, which can effectively achieve a trade-off result and comprehensive optimal solution. Figure 9 shows the optimization results of the three optimization objectives via the above method. It can be clearly seen that the feasible points are distributed in a three-dimensional space composed of the three objectives, and where all of the points are satisfied with the boundary constraints proposed in step 2. The final result of the optimal design point is marked with a red pentagonal dot. Based on the optimization results, the corresponding values of the three optimization objectives and the design variables in step 2 are listed in Table 4.

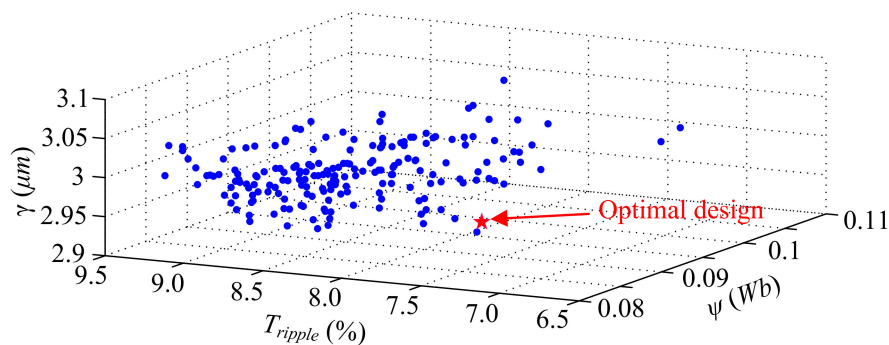


Figure 9. The optimization results of the three optimization objectives in step 2.

Table 4. Optimal design in step 2.

Variables/Objectives	Initial Value	Optimal Value
$a$ (mm)	4.0	4.8
$R$	0.4	0.45
$\beta_{pm}$ ( $^{\circ}$ )	24	20
$B_{po}$ ( $^{\circ}$ )	20	16.2
$T_{ripple}$ (Nm)	11.8	7.2
$\gamma$ ( $\mu\text{m}$ )	3.4	2.9
$\psi$ (Wb)	0.091	0.082

#### 4. Performance Analysis

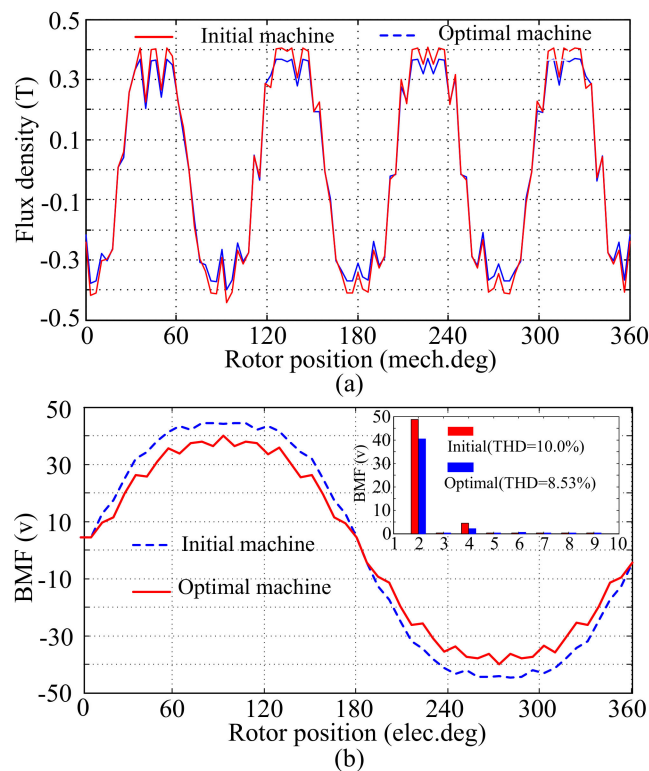
In order to demonstrate the effectiveness of the electromagnetic–mechanical coupling optimization strategy and the reasonability of the investigated machine, the corresponding optimal design results have been demonstrated via simulation analysis. In this section, based on the finite-element analysis and the static structural analysis, some representative electromagnetic performances and the mechanical performances of the machine before and after optimization are evaluated and compared.

Figure 10a compares the corresponding air-gap flux density of the machines before and after optimization under a no-load condition. It can be seen that variation trends of the air-gap density of the two machines are almost the same. Due to the fact that the usage of a permanent magnet is reduced, the optimal machine has a lower air-gap flux density. It accordingly produces a lower no-load back electromotive force (back-EMF) value as shown in Figure 10b. That is, the optimal machine will be more vulnerable to its magnetic field weakening with the same weakening current. Furthermore, the fast Fourier analysis of the back-EMFs is also conducted in Figure 10b. It can be obtained that the initial machine possesses a higher fundamental harmonic than the optimal machine, but the optimal machine has lower total harmonic content (THD) values. This means that the optimal machine has relatively more sinusoidal back-EMF waveform, which is helpful for machine control operation.

The torque performances of the machine are studied in Figure 11. From Figure 11a, it can be noticed that the total torque before and after optimization is almost equal, and the main changes are focused on the proportion of the reluctance torque and PM torque. After optimization, the machine reluctance torque increases obviously from 22 to 23.8 Nm, whereas the PM torque decreases slightly after optimization. This means that the optimized machine can use less PM to achieve a larger torque. From Figure 11b, it can be seen that the torque ripple of the machine decreases significantly after optimization, which is expected to provide beneficial conditions for the smooth drive of the machine for EV application.

In addition to low speed and high torque, electric vehicles are expected to have a wide range of constant power speed regulation. Thus, the corresponding power-speed characteristics are investigated. From Figure 12, in the low-speed constant-torque region, the output power of the initial PM machine and optimal machine are almost the same. Nevertheless, in the high-speed constant-power region, although the output power of both machines shows downward trends, the optimal machine power

decreases more slowly. This shows that the optimal machine is more suitable for the wide speed regulation of electric vehicles.



**Figure 10.** No-load performances before and after optimization. (a) Air-gap flux density. (b) Back-EMF and spectral analysis.

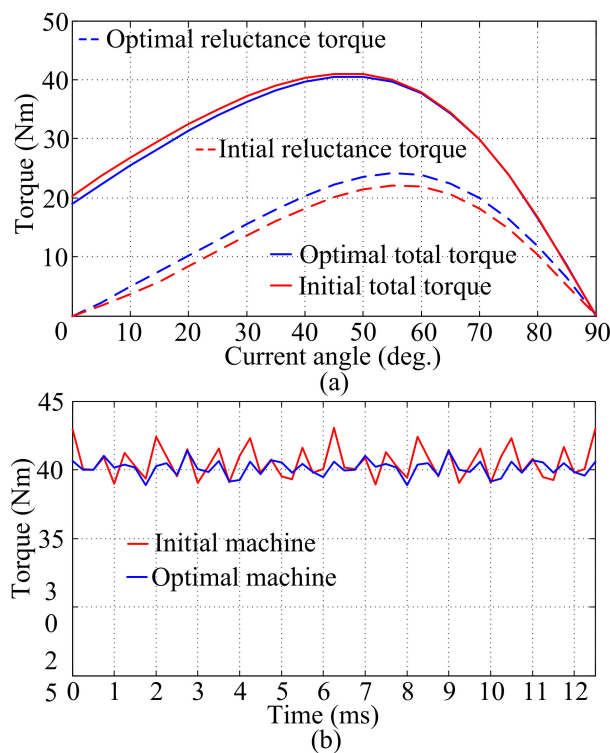


**Figure 11.** Torque performances of the machine before and after optimization. (a) Torque vs. current angle. (b) Torque ripple characteristics.

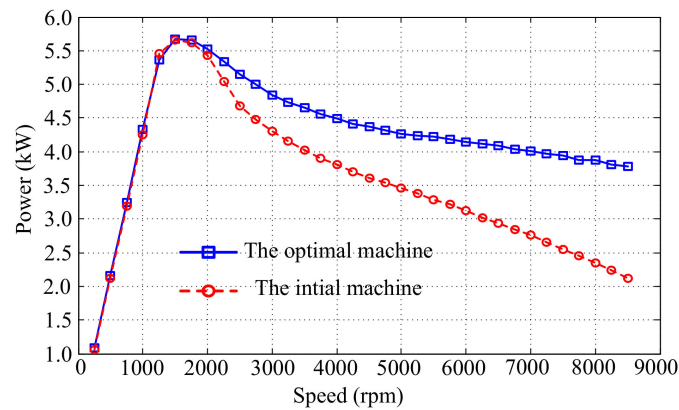


**Figure 12.** The power-speed characteristics of the initial machine and optimal machine.

Figure 13 depicts the maximum mechanical deformation and maximum mechanical stress versus the rotor speed. Compared with the initial machine, both maximum deformation and mechanical stress are obviously decreased at each rotor speed. In particular, the maximum deformation and maximum stress in maximum rotor speed decline from 3.4 to 3.0  $\mu\text{m}$  and 107.5 to 71.2 Mpa, respectively. Therefore, it can be noted that this optimization strategy can not only improve the electromagnetic performances of the machine but also improve the mechanical performances of the machine when operating at a high speed.

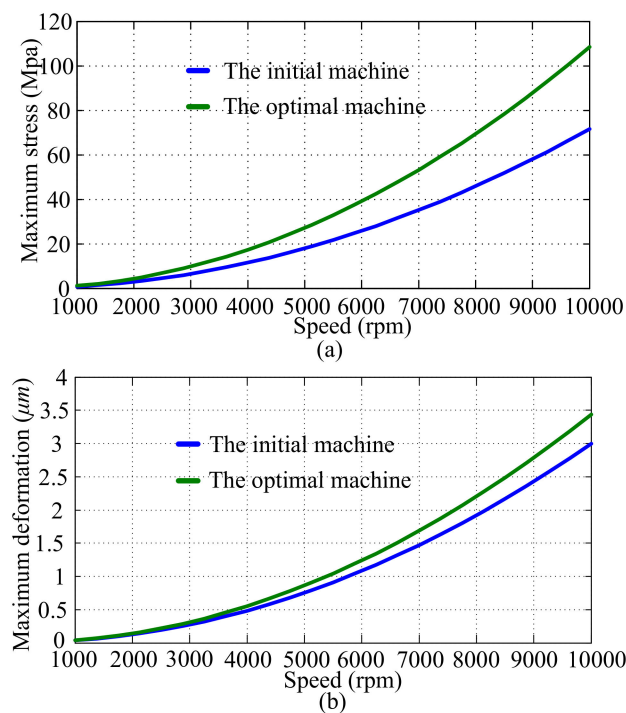


**Figure 13.** Rotor mechanical performances of the machine before and after optimization: (a) maximum stress vs. speed; (b) maximum deformation vs. speed.

The efficiency maps of the machines are also evaluated and compared by finite element analysis (FEA), and the results are shown in Figure 14. By comparing the two efficiency maps, it can be found that the speed range of the machines before and after optimization is relatively close, and both the initial and optimal machine can reach a maximum speed of 8000 rpm. However, in the whole speed range, the distribution of efficiency is different. As for the optimal machine, it can maintain a 96% efficiency to its 4800 rpm and also presents a greater range of high efficiency. When comparing the efficiency of the high-speed region, the difference is even more pronounced. For instance, at the speed

point of 6000 rpm, the optimal machine can operate at a maximum efficiency of 92.8, but the initial machine is only 90.9. Therefore, we can make the optimal machine operate with a higher efficiency in medium-to-high speed, which is more advantageous for EV acceleration in high-speed operation.

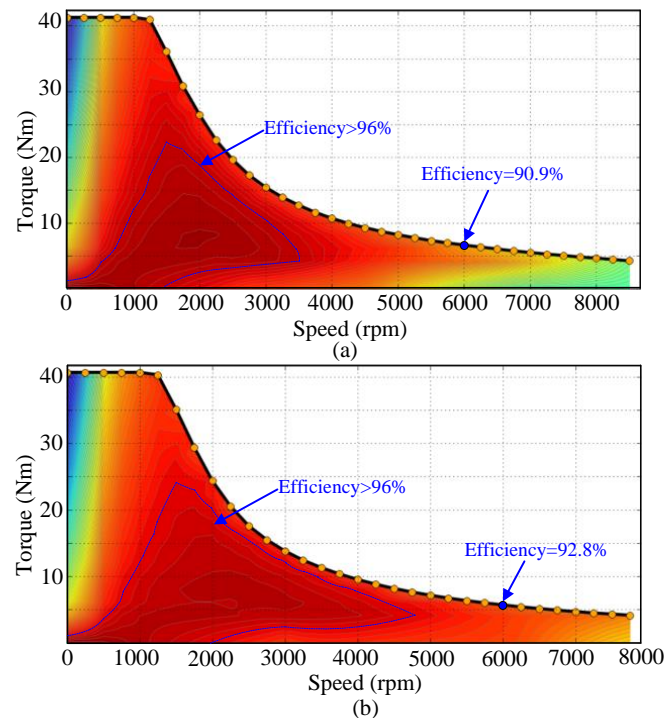


**Figure 14.** Efficiency characteristics by FEA: (a) the efficiency map of the initial machine; (b) the efficiency of the optimal machine.

## 5. Conclusions

In this paper, an IPM synchronous machine with multiflux barriers is proposed for high-speed industrial application, such as EVs. In the process of electromagnetic–mechanical coupling optimization design, the partitioning optimization technique is adopted in rotor barrier design, which can be used as a reference for the multiple-barrier machine design. Through optimization, the proportion of the reluctance torque is increased on the premise that the total torque does not decrease. Meanwhile, both mechanical stress and mechanical deformation at the maximum speed are reduced to an acceptable level. By comparing efficiency characteristics before and after optimization, we can make the optimal machine operate with a higher efficiency in medium-to-high speed, which is more advantageous for EV acceleration in high-speed operation. That is, the electromagnetic and mechanical coupling optimization strategy is validated as effective in dealing with the IPM synchronous machines with multiflux barriers.

**Author Contributions:** W.W. is the main author of this manuscript who implemented the research and performed the analysis. X.Z. and Z.X. conceived of the idea of the research and provided guidance and supervision. Q.C. and F.Z. assisted in the implementation of the research and provided constructive suggestions for the construction of this article. All the authors made a significant contribution to the work. All authors have read and agree to the published version of the manuscript.

**Funding:** This work was supported in part by the Teachers Research Foundation of Changshu Institute of Science and Technology of KYZ201900040Q, in part by the Ningbo Natural Science Foundation of 2017A610083, and in part by the Natural Science Foundation of Zhejiang Province of LY17E050006.

**Conflicts of Interest:** The authors declare no conflict of interest.

## Nomenclature

$T_{rel}$	Reluctance torque
$T$	Maximum stress
$T_{ripple}$	Torque ripple
$R_{ib1}$	Bridge width
$h_1$	Low barrier thickness
$\beta_{po}$	Starting angle of arc PM
$R$	Proportion coefficient of minor and major axis
$a$	Length of the major axis of the elliptical barrier
$y/f(x)$	Optimization objective
$S(x_i)$	Sensitivity index
$\xi$	Saliency ratio
$\psi$	Flux linkage
$\gamma$	Maximum deformation
$R_{ib2}$	Rid width
$h_2$	Upper barrier thickness
$\beta_{pm}$	Radian of the PM in barrier
$x_i$	Optimization variable
$T_{out}$	Output torque

## References

- Cheng, M.; Hua, W.; Zhang, J.; Zhao, W. Overview of stator-permanent magnet brushless machines. *IEEE Trans. Ind. Electron.* **2011**, *58*, 5087–5101. [[CrossRef](#)]
- Zhu, X.Y.; Xiang, Z.X.; Quan, L.; Wu, W.Y.; Du, Y. Multimode optimization design methodology for a flux-controllable stator permanent magnet memory motor considering driving cycles. *IEEE Trans. Ind. Electron.* **2018**, *65*, 5353–5366. [[CrossRef](#)]
- Zhang, P.; Dan, M.L.; Demerdash, N.A.O. Saliency Ratio and Power Factor of IPM Motors With Distributed Windings Optimally Designed for High Efficiency and Low-Cost Applications. *IEEE Trans. Ind. Appl.* **2016**, *52*, 4730–4739. [[CrossRef](#)]
- Jung, J.W.; Lee, B.H.; Kim, D.J.; Hong, J.P.; Kim, J.Y.; Jeon, S.M.; Song, D.H. Mechanical stress reduction of rotor core of interior permanent magnet synchronous motor. *IEEE Trans. Magn.* **2012**, *48*, 911–914. [[CrossRef](#)]
- Chai, F.; Li, Y.; Liang, P.X.; Pei, Y.L. Calculation of the maximum mechanical stress on the rotor of interior permanent-magnet synchronous motor. *IEEE Trans. Ind. Electron.* **2016**, *63*, 3420–3432. [[CrossRef](#)]
- Zhu, X.Y.; Fan, D.Y.; Xiang, Z.X.; Quan, L.; Hua, W.; Cheng, M. Systematic multi-level optimization design and dynamic control of less-rare-earth hybrid permanent magnet motor for all-climatic electric vehicles. *Appl. Energy* **2019**, *253*, 113549. [[CrossRef](#)]
- Zhu, X.Y.; Huang, J.; Quan, L.; Xiang, Z.X.; Shi, B. Comprehensive Sensitivity Analysis and Multiobjective Optimization Research of Permanent Magnet Flux-Intensifying Motors. *IEEE Trans. Ind. Electron.* **2019**, *66*, 2613–2627. [[CrossRef](#)]
- Uddin, N.; Chy, M. On-Line Parameter Estimation Based Speed Control of PM AC Motor Drive in Flux Weakening Region. *IEEE Trans. Ind. Appl.* **2008**, *44*, 1486–1494. [[CrossRef](#)]
- Boldea, I.; Tutelea, L.N.; Parsa, L.; Dorrell, D. Automotive Electric Propulsion Systems with Reduced or No Permanent Magnets: An Overview. *IEEE Trans. Ind. Electron.* **2014**, *61*, 5696–5711. [[CrossRef](#)]
- Vagati, A.; Boazzo, B.; Guglielmi, P.; Pellegrino, G. Design of ferrite-assisted synchronous reluctance machines robust toward demagnetization. *IEEE Trans. Ind. Appl.* **2014**, *50*, 1768–1779. [[CrossRef](#)]
- Wu, W.Y.; Zhu, X.Y.; Quan, L.; Du, Y.; Xiang, Z.X.; Zhu, X. Design and analysis of a hybrid permanent magnet assisted synchronous reluctance motor considering magnetic saliency and PM usage. *IEEE Appl. Supercond.* **2018**, *28*, 1–6. [[CrossRef](#)]
- Bianchi, N.; Fornasiero, M.; Soong, W. Selection of PM flux linkage for maximum low-speed torque rating in a PM-assisted synchronous reluctance machine. *IEEE Trans. Ind. Appl.* **2015**, *51*, 3600–3608. [[CrossRef](#)]
- Limsuwan, N.; Kato, T.; Akatsu, K.; Lorenz, R.D. Design and evaluation of a variable-flux flux intensifying interior permanent magnet machine. *IEEE Trans. Ind. Appl.* **2014**, *50*, 1015–1024. [[CrossRef](#)]

14. Zhu, X.Y.; Yang, S.; Du, Y.; Xiang, Z.X.; Xu, L. Electromagnetic performance analysis and verification of a new flux-intensifying permanent magnet brushless motor with two-layer segmented permanent magnets. *IEEE Trans. Magn.* **2016**, *52*, 8204004. [[CrossRef](#)]
15. Limsuwan, N.; Shibukawa, Y.; Reigosa, D.D.; Lorenz, R.D. Novel design of flux-intensifying interior permanent magnet synchronous machine suitable for self-sensing control at very low speed and power conversion. *IEEE Trans. Ind. Appl.* **2011**, *47*, 2004–2012. [[CrossRef](#)]
16. Nardo, M.D.; Calzo, G.L.; Galea, M.; Gerada, C. Design Optimization of a High-Speed Synchronous Reluctance Machine. *IEEE Trans. Ind. Appl.* **2018**, *54*, 233–243. [[CrossRef](#)]
17. Lei, G.; Wang, T.; Guo, Y.G.; Zhu, J.G.; Wang, S.H. System-level design optimization methods for electrical drive systems deterministic approach. *IEEE Trans. Ind. Electron.* **2014**, *61*, 6591–6602. [[CrossRef](#)]
18. Lei, G.; Wang, T.S.; Zhu, J.G.; Guo, Y.G.; Wang, S.H. System-level design optimization method for electrical drive systems-robust approach. *IEEE Trans. Ind. Electron.* **2015**, *62*, 4702–4713. [[CrossRef](#)]



© 2020 by the authors. Licensee MDPI, Basel, Switzerland. This article is an open access article distributed under the terms and conditions of the Creative Commons Attribution (CC BY) license (<http://creativecommons.org/licenses/by/4.0/>).